Studying turbulence in a fluid with background damping

P. Bajaj,[1,*] A. Ivlev,[2] C. Räth,[3] and M. Schwabe[4]

[1]*Institut für Materialphysik im Weltraum, Deutsches Zentrum für Luft- und Raumfahrt (DLR), 51147 Köln, Germany*

[2]*Max-Planck-Institut für Extraterrestrische Physik, 85741 Garching, Germany*

[3]*Institut für KI Sicherheit, Deutsches Zentrum für Luft- und Raumfahrt (DLR), 89081 Ulm, Germany*

[4]*Deutsches Zentrum für Luft- und Raumfahrt (DLR), Institut für Physik der Atmosphäre, 82234 Oberpfaffenhofen, Germany*

(Received 6 December 2022; accepted 26 April 2023; published 20 June 2023)

In this experimental paper, we demonstrate that turbulence can develop in a fluid system with background damping. For that purpose, we analyze dust acoustic waves, self-excited in a fluid complex plasma where the motion of individual microparticles was recorded with a high-speed video camera. We use the Wiener-Khinchin theorem to calculate the kinetic spectrum during different phases of the highly nonlinear periodic wave motion and show that a turbulent cascade develops at the phases of highest particle compression. We demonstrate that the energy cascade occurs despite the presence of a damping force due to the background neutral gas.

DOI: 10.1103/PhysRevE.107.064603

I. INTRODUCTION

Turbulence occurs in dissipative systems far away from thermodynamic equilibrium with many degrees of freedom. It is a phenomenon observed in a multitude of cases beyond ideal incompressible fluids ranging from microscopic oscillations in solids and plasmas to macroscopic processes during planet formation [1,2], and encompassing systems as diverse as vibrating elastic plates [3–5] and active particles [6]. Here, we study turbulence using a fluid complex plasma by analyzing the motion of micrometer-sized particles in dust acoustic waves (DAWs).

Complex (or dusty) plasmas are nanometer to micrometer-sized solid particles embedded in the plasma environment of ions, electrons, and neutrals. The microparticles attain a very high negative charge due to the higher mobility of electrons than ions [7] and exhibit collective effects, such as the formation of solid or liquidlike phases in complex plasmas or the self-excitation of DAWs at a suitably low pressure of the neutral gas [8]. Dusty plasmas are found in nature in the form of comet tails, planetary rings, or noctilucent and interstellar clouds [9–11]. Due to the microparticles' low charge-to-mass ratio and relatively large size, their motion can be traced using high-speed optics. This makes complex plasmas ideal to study collective phenomena, such as turbulence at the atomistic (kinetic) level.

In complex plasmas, the self-excitation of DAWs [12] occurs due to the ion-dust streaming instability, i.e., the motion of ions past the microparticles, which are levitated above the bottom electrode where the force of gravity balances the electric field force. DAWs were first predicted by Rao *et al.* [13] and have since been extensively studied theoretically [14] as well as experimentally [15–17]. The DAWs usually move in the direction of the ion flow.

DAWs have been used in the past to study turbulence in complex plasmas [18–28]. The aim of the present paper is to investigate under which conditions turbulence develops in a fluid complex plasma despite the presence of the Epstein friction force that could prevent the formation of the turbulent energy cascade. As the neutral gas atoms collide with the microparticles, they exert a force called the neutral drag force or Epstein friction [29] on the microparticles, which leads to a reduction of the microparticle velocity.

Turbulence has been observed in many natural systems with unique dissipation mechanisms, for instance, surface gravity waves [30], capillary waves on a liquid surface [31,32], quantum turbulence in two-fluid regime [33], near-wall turbulence [34], turbulence near the solar nebula [35], or solar wind turbulence [36], magnetohydrodynamics turbulence in partially ionized gas of the interstellar medium [37,38] or with snowdrift where snow particles damp the turbulence in the atmosphere [39], and even auroral ionospheric turbulence [40].

In this article, we demonstrate that it is feasible to study turbulence using fluid complex plasmas despite the presence of the Epstein damping force. Complex plasmas are particularly well suited as a model system to study turbulence because they enable the resolution of the individual microparticles in a turbulent interaction. This, in principle, makes it possible to study the entire space-time structure of the turbulent field. It is only possible to study continuous media using regular fluid systems. However, complex plasmas provide a unique opportunity to study different kinetic behaviors in nature even at the smallest length scales. Hence, complex plasmas can be used to study the link between different fields of physics. They serve as a powerful tool to investigate fluid flows at (effectively) nanoscales, including the mesoscopic collective phenomena to the microscopic dynamics of individual particles along with several linear, nonlinear, critical, etc., processes on atomistic scales that were not accessible previously.

In this paper, apart from demonstrating that the background damping does not necessarily prevent the formation of the turbulent cascade, we investigate the isotropy and dependence of turbulence on the wave phase in our system. We introduce

*prapti.bajaj@dlr.de

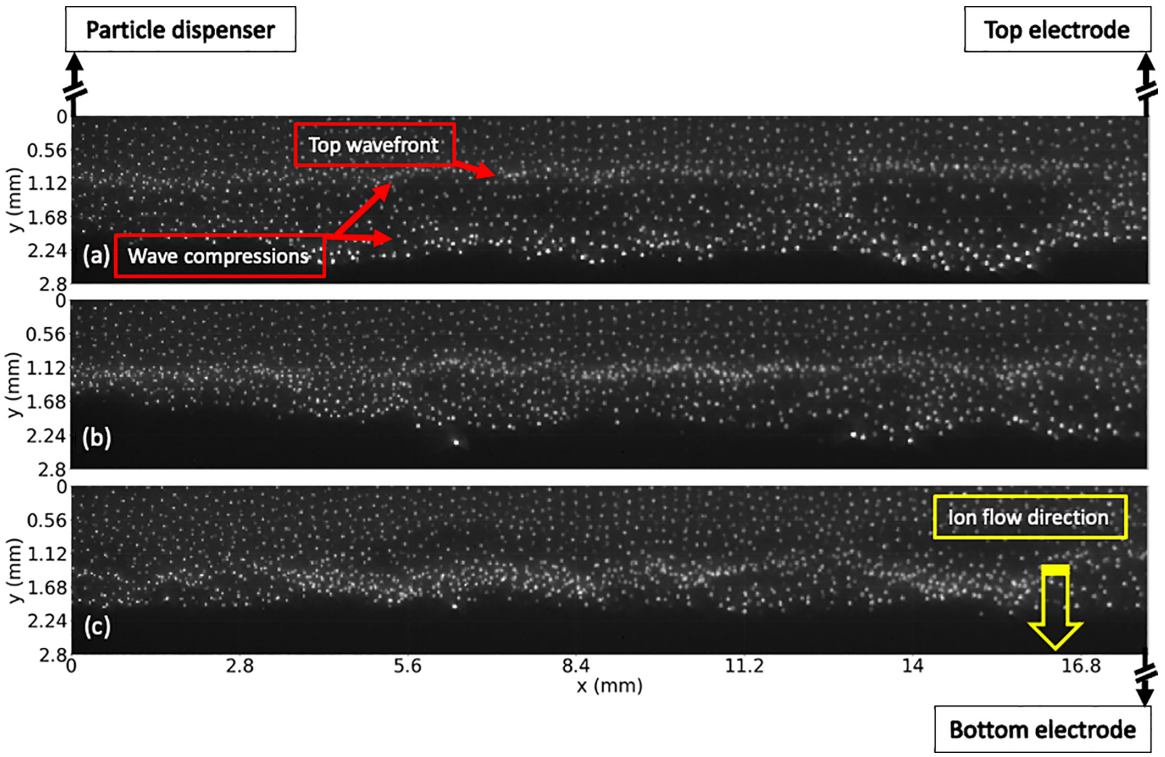

FIG. 1. Three characteristic snapshots illustrating a collision of nonlinear DAWs propagating in the vertical (y) direction (same as the direction of ion flow). The time interval between image (a) and (b) is 27.5 ms and between (b) and (c) 10.5 ms.

the experimental setup in Sec. II and the analytical methods and underlying theoretical descriptions in Sec. III. After this, we present the analytical results in Sec. IV and conclude in Sec. V.

II. EXPERIMENT

We used a modified ground-based version of the PK-3 Plus laboratory [41,42] that was originally developed for microgravity research. An up-to-date schematic diagram for this setup can be found in a previous publication [43]. Since the experiments were performed on ground under the influence of gravity, the microparticles were pushed into the bottom sheath and were subject to ion drag force directed downwards. A capacitively coupled radio-frequency plasma chamber forms the heart of the laboratory. A plasma is generated by a sinusoidal signal with a frequency of 13.56 MHz on the electrodes. We used argon at a pressure of 23 Pa with a flow rate of 0.2 sccm standard cubic centimeters per minute (sccm), and a voltage of 56 V_{pp} on the electrodes. We injected monodisperse melamine formaldehyde spheres of mass density 1510 kg/m^3 and a diameter of 4.4 μm. A laser with a wavelength of 532 nm and a power of 45 mW illuminated the microparticles in a vertical plane. Their motion was tracked using video camera Photron Fastcam-1024 PCI at a speed of 2000 frames per second with a field of view of 640 × 640 pixel^2 at a spatial resolution of 28 μm/pixel.

After the microparticles were injected, we started observing unstable waves in the microparticle cloud. Figure 1 shows experimental snap shots at three instances of time during the downwards propagation of the waves. Each microparticle inside the laser plane is visible as a white dot. Some brighter particles in the bottom of the cloud are probably agglomerates [44].

III. THEORY

The most typical states of a statistical system far from thermodynamic equilibrium are determined by the flux of energy (or any other conserved quantity) through different spatial and temporal scales, rather than temperature or other thermodynamic potentials [1,2]. The most common example for this is the self-similar cascade of energy through scales, i.e., as a sequence of transfers from larger eddies to successively smaller ones until energy is dissipated through viscous forces [45]. In this case, the advection term in the Navier-Stokes equation provides a characteristic inverse timescale, the inverse eddy turnover time,

$$\tau_{\rm cas}^{-1} = kv(k), \tag{1}$$

where k is the wave number (inversely proportional to the characteristic length scale) and $v(k)$ is the fluid velocity as a function of the wave number. The velocity $v(k)$ can be used to obtain the power spectrum defined as

$$E(k) \equiv v^2(k)/2k, \tag{2}$$

which is equivalent to the energy density, i.e., energy per unit wave number and unit mass. Using this, we obtain the rate of cascade of energy ($\tau_{\rm cas}{}^{-1}$) as

$$\tau_{\rm cas}{}^{-1} = k\sqrt{2kE(k)}. \tag{3}$$

As discussed above, the microparticles in complex plasmas experience a background friction force due to their collisions with neutral gas atoms, the neutral drag or Epstein force [7,29]. It is given as

$$F_n = -m_d \beta v_d, \tag{4}$$

where m_d is the mass of the microparticles, v_d is the velocity of the microparticles, and β is the Epstein friction coefficient or the damping rate coefficient defined as

$$\beta = \delta \frac{4\pi/3}{3} \frac{n_n m_n u_n}{m_d} {r_d}^2, \tag{5}$$

with $u_n = \sqrt{8 k_B T_n / \pi m_n}$, the number density of gas atoms n_n, the microparticle radius r_d, the mass of the neutral gas atoms m_n, the temperature of the neutral atoms T_n, and the microparticle mass m_d. The value of the coefficient δ depends on the collision mechanism, varying between 1.0 for specular reflection and 1.442 for diffuse reflection [29]. We use the value of $\delta = 1.44 \pm 0.19$ for our calculations as measured using a vertical resonance method [46]. Using Eq. (5), we calculate the value of the damping rate in our system as $63.58 \pm 0.13\ \mathrm{s}^{-1}$. It is interesting to note here that the "damping frequency" ($\approx$10 Hz) is about 0.3 times the frequency of the DAWs ($\approx$30 Hz [43]).

In order to study whether turbulent cascades can form in our system despite the presence of the background neutral drag force, we compare the rate of cascade with the damping rate of the system. If the cascade rate is higher than the damping rate, the development of turbulence is possible.

In order to analyze our system, we use the Wiener-Khinchin theorem (WKT) [47–50], which states that the correlation function $\Gamma(l)$ and the power spectrum $E(k)$ are Fourier transforms of each other [1]. The correlation function is defined as

$$\Gamma(l) \equiv \langle [\vec{v}(\vec{r}) \cdot \vec{v}(\vec{l} - \vec{r})] \rangle, \tag{6}$$

where $l = |\vec{l}|$ is the distance between two particles at position $\vec{r}$ and $\vec{l} - \vec{r}$, $\vec{v}$ is the instantaneous velocity of the particles at their respective positions, and $\langle\,\rangle$ symbolizes the average over each interparticle distance. This theorem is applicable to any stochastic process with a wide-sense stationarity as explained in detail by Wiener himself [47]. From a mathematical point of view, any variable, such as the particle velocity in our system, can be used to calculate the energy spectrum by Fourier transforming its autocorrelation function. For an isotropic system, the Fourier transform of the correlation function gives the three-dimensional (3D) power spectrum defined as [1]

$$E^{3D}(k) = 4\pi k^2 \int \Gamma(\vec{l}) \exp^{-i2\pi \vec{k} \cdot \vec{l}}\, d\vec{l}. \tag{7}$$

To study our anisotropic system, we use the discrete Fourier transform of the one-dimensional (1D) correlation function (in the y direction/wave propagation direction) to study the dissipation of energy. For this, we discretize the entire range of interparticle distances into N bins. This gives us discrete bins of interparticle distances as $l_m = \frac{mL}{N} \equiv m\Delta$, where m is a particular bin such that $m = 0, \ldots, N-1$, and Δ is the bin size. Here, we use $\Delta = 0.028$ mm (= 1 pixel) and $N = 95$ bins with a total length extent of $L = N\Delta = 2.66$ mm in the vertical (y) direction. This gives us $\Gamma_m \equiv \Gamma(l_m)$ as the correlation function for a particular bin of interparticle distance l_m. Using this, we get the discrete Fourier transform of the correlation function as

$$E^{1D}(k) \equiv \Delta \left| \sum_{m=0}^{N-1} \Gamma_m \exp^{-i2\pi mk\Delta} \right|. \tag{8}$$

IV. RESULTS

We follow the microparticles as they move from one frame to another using the python package TRACKPY [51]. Please note that some particles are lost in the tracking process as they move out of the laser plane, and that the distinction of individual microparticles inside the dense wave fronts is not always possible. After tracking the microparticles, we find the two-dimensional velocity of each particle as it travels from one frame to another, i.e., $\vec{v}_i(\vec{r}, t)$, where i is the particle ID, $\vec{r}_i(x, y)$ is the Cartesian coordinate of the particle, and t is time. In a previous publication [43], we use a plot of the average particle velocity in a small region of space as a function of time to demonstrate that this method results in sensible values even inside the wave fronts for these particles that were traceable. However, for the following, we would like to point out that the resolution at small length scales, comparable to the interparticle distance $d = 0.11$ mm, is too poor to produce reliable analytical results. We still present results at these scales to provide a comparison with the other length scales in the system. Any knowledge of the spectra at these small length scales could be useful for the study of turbulence as most conventional fluid dynamic systems do not allow the possibility to resolve these scales.

We note that our system is highly anisotropic since the wave fronts propagate in the y direction. This leads to higher particle velocities and, thus, higher kinetic energies in the k_y space than in the k_x space. Also, the scaling laws are different for the two observable dimensions. Henceforth, we restrict our analysis to the direction of the propagation of the DAWs, i.e., in the y direction.

Figure 1 shows three experimental snap shots that help to understand the experimental situation near the bottom of the particle cloud, the area of interest. Wave fronts move from the top of the cloud towards the bottom. At the time instance shown in Fig. 1(a), two wave fronts can be seen, labeled as "wave compressions." The waves carry the particles due to electrostatic force. At the bottom edge of the microparticle cloud, the wave fronts push the microparticles into the sheath and then dissolve. This can already be observed in the lower wave front in Fig. 1(a), which is less strongly compressed than the top wave front.

After this, the particles that were previously contained in the bottom wave front begin to move upwards towards the approaching top wave front as in Fig. 1(b). Finally, the bottom particles collide with the top wave front, leading to the highest compression as shown in Fig. 1(c). This leads to very strong interparticle interactions, similarly as a collision between two wave fronts would.

Next, the remaining wave front in Fig. 1(c) then propagates further downwards, and we see another wave front self-excited further up in the microparticle cloud, similar as in Fig. 1(a). This repeats cyclically in our system. This allows

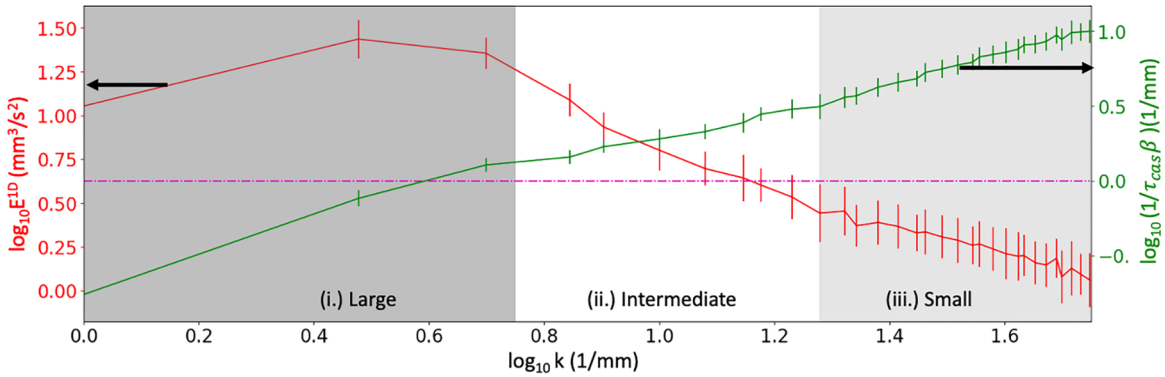

FIG. 2. The calculated power spectrum (red, left axis) and the ratio of the rate of energy cascade $\tau_{\text{cas}}{}^{-1}$ to the rate of Epstein damping β (green, right axis) for the wave phase similar as shown in Fig. 1(c), obtained by averaging spectra in 51 instances of time corresponding to the same wave phase. The indicated regions of wave numbers are as follows: (i) $k = (0–5.6)$ mm^{-1} (dark gray, corresponding to spatial scales larger than the DAW wavelength), (ii) $k = (5.6–18.96)$ mm^{-1} (white, corresponding to intermediate spatial scales between the wavelength and the width of the wave compression), and (iii) $k = (18.96–56)$ mm^{-1} (light gray, corresponding to small spatial scales between the width of the wave compression and the typical interparticle distance). The pink dashed-dot line shows the case when the cascade rate ($\tau_{\text{cas}}{}^{-1}$) is equal to the damping rate (β).

us to obtain better statistics by averaging experimental measurements obtained during the same wave phase.

It is only possible that turbulence develops in a system with background damping if the cascade rate is higher than the damping rate. Figure 2 shows the power spectrum (red) and the ratio of the logarithm of the cascade rate to the damping rate (green) at a particular phase of the wave propagation corresponding to the situation shown in Fig. 1(c) when the particle number density inside the wave front is the largest due to the collision with the reflected particles. The damping rate was calculated in Sec. III, the cascade rate using Eq. (3) and the energy spectra obtained with the WKT, discussed in Sec. III. The figure shows that the cascade rate (green) is higher than the damping rate (magenta dash-dot line) by around one order of magnitude at small spatial scales. In this figure, the error bars are the standard deviations obtained from the statistical averaging of energy spectra at different time instances within the same wave phase.

Three regions of wave numbers are marked: (i) large spatial scales (dark gray), larger than the wavelength of the DAW, $\lambda = 1.12$ mm, (ii) intermediate length scales (white) between λ and the width of the thinnest wave compression ($= 0.33\,\text{mm}^{-1}$), and (iii) small length scales (light gray) between the width of the wave compression and the typical interparticle distance in our experiment, $d = 0.112$ mm.

The magenta dashed-dot line indicates where the damping rate β is equal to the cascade rate. The cascade rate is higher than the damping rate for the intermediate and small length scales (white and light-gray regions) and, thus, turbulence can develop in these wave number regions. We have also confirmed that this is true for all the frames individually within this phase and for phases other than shown here. The energy spectra of the other phases along with exemplary experimental snap shots at those phases are presented in the Supplemental Material [52]. Thus, we conclude that turbulence can be observed in our experiment for intermediate and small length scales. We also studied the impact of artificial pixel locking [53,54] and found that even after introducing it externally, there is minimal impact on energy spectrum. Hence, pixel locking has negligible effects on the energy spectrum in our experimental conditions.

Next, to get a clearer picture of the changes in energy flux during the various wave phases and wave number regions, we consider the changes in the power spectra. For this, we make a least squares fit to the energy spectrum in each of the regions of interest, i.e., region (ii) (intermediate scale) or (iii) (small length scale) at every wave phase. Due to the lack of theoretical models of turbulence in complex plasmas, the expected slope of the energy spectrum is not known in advance. Thus, we perform a polynomial fit of the first degree using the PYTHON library NUMPY, and then extract the goodness of fit value, r^2. We only fit with first-order polynomial and can already find reasonably good results using the threshold of $r^2 \geqslant 0.9$. The resulting slopes Φ are shown in Fig. 3(a) (blue, gray, corresponding to intermediate, small length scales, respectively) along with the resulting coefficient of determination r^2, as a measure of goodness of fit. The slope Φ is defined as

$$\Phi = \frac{d\,\log E}{d\,\log k}. \tag{9}$$

The coefficient of determination is defined as the proportion of variation in the fitted energy spectrum to the actual energy spectrum,

$$r^2 = 1 - \frac{\sum_i e_i^2}{\sum_i \left[E_i^{1\text{D}}(k) - E_m^{1\text{D}}\right]^2} \tag{10}$$

where $e_i = E_i^{1\text{D}}(k) - \hat{E}_i^{1\text{D}}(k)$ is the error (residual) between the actual and fitted power spectrum values i, $\hat{E}_i^{1\text{D}}(k)$ are the fitted power spectrum values, and $E_m^{1\text{D}}$ is the mean power spectrum value. The calculated r^2 is plotted as a function of time in Fig. 3(b). The three snapshots on the top of Fig. 3 show three examples of wave propagation same as shown in Fig. 1. The error bars in Fig. 3 are the standard deviations in

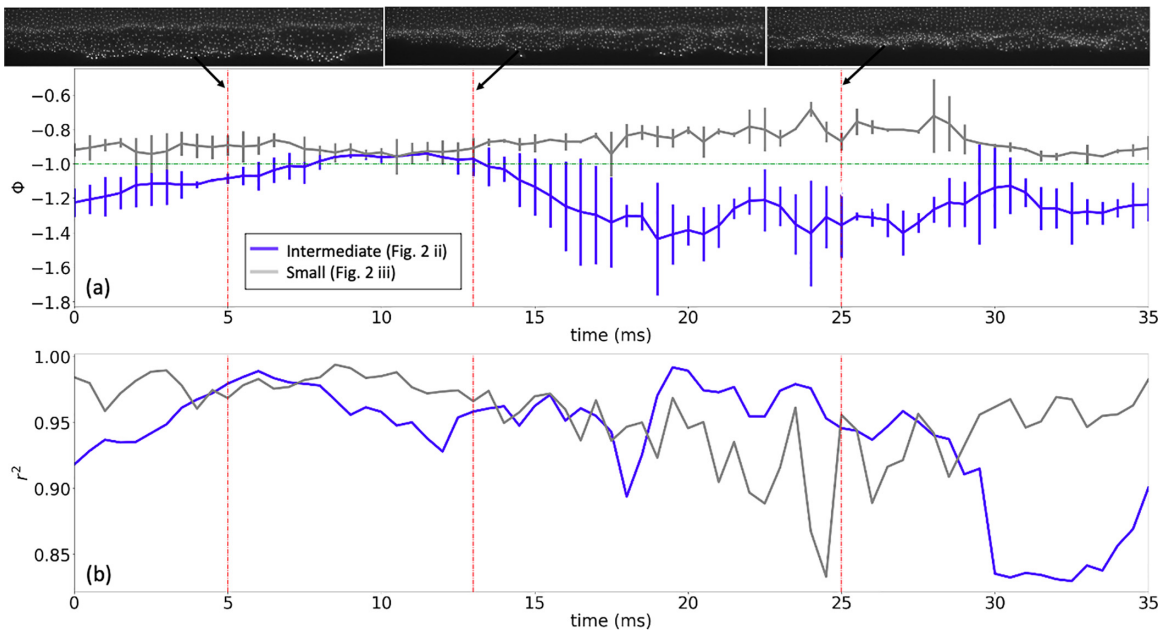

FIG. 3. (a) Periodic variation of the slope (Φ) resulting from fits for various wave number regions shown in Fig. 2 as a function of time during one wave period (blue: intermediate scales, gray: small scales, green dashed-dot: $\Phi = -1$). The vertical lines show the standard deviation of the calculated mean slope values at the same wave phase. (b) r^2 values [Eq. (10)] as measures of the goodness of the fit as a function of wave phase. (Top) Experimental snapshots from Figs. 1(a)–1(c) (left to right).

the values of fit performed on energy spectra of each wave phase.

The particle motion is driven mainly by the bulk electric field, for the phases illustrated in Figs. 1(a) and 1(b). During these instances, the slope of the power spectrum Φ in the intermediate length scales is close to −1.

In contrast, in the phase corresponding to Fig. 1(c), the particles collide and thus interact strongly with each other. In this region the slope Φ is around −1.3 in the intermediate length scales (between the wavelength and the width of a wave compression) with r^2 values above 0.85. This is the region where turbulent cascades could develop. Hence, we conclude that nonstationary turbulence can be observed with a scaling law of about –1.3 for time instances when the particles traveling from the bottom and colliding with the top wave front form a region of high compression. Also, we conclude that this law is observable at the length scales indicated as intermediate in the previous Fig. 2.

On the small length scales (gray lines) the measured Φ has a magnitude smaller than 1. This is due to the poor resolution of these length scales (smaller than 0.33 mm) as also indicated by the large error bars because of the limited resolution of the experimental system.

V. CONCLUSION

To conclude, in this paper, we demonstrated that it is possible to study turbulence using fluid complex plasmas even in the presence of background damping, which has relevance to many other fields in which turbulence is studied in the presence of damping.

We also investigated in detail how the dynamic properties of the system changed with the propagation of DAWs. The waves formed near the top of the microparticle cloud and propagated downwards toward the lower electrode. Upon approaching the bottom sheath, the microparticles were reflected and collided with the following wave front. During this situation the particles strongly interacted with each other, and turbulent cascades formed, as indicated by the change in slope of the power spectrum from –1 to –1.3. Our research suggests that in highly collisional systems with waves and particles colliding with each other, it is possible to observe a turbulent energy cascade even in the presence of a background damping force. In the future, we will study this onset of turbulence in more detail by making the waves more nonlinear and by enlarging the region of wave propagation. This can be achieved by changing a physical parameter in the chamber to observe more wave fronts than observed in the reported experiment. With a larger number of wave fronts, we will be able to study the spectra in more detail as the domain of length scales will increase. We will also study the influence of physical parameters, such as particle size or wavelength, on the onset of turbulence and the energy spectrum.

ACKNOWLEDGMENTS

We thank P. Huber and D. Mohr for offering IT help during the course of this project; T. Hagl and C. George for experimental support; and H. Thomas for his input and support. We would also thank M. Sperl for careful reading of the paper and useful suggestions. We acknowledge funding of this work in the framework of the Nachwuchsgruppenprogramm im DLR Geschäftsbereich Raumfahrt.

[1] U. Frisch, *Turbulence* (Cambridge University Press, Cambridge, UK, 1995).
[2] S. Nazarenko, *Wave Turbulence* (Springer-Verlag GmbH, Berlin, 2011).
[3] N. Mordant, Phys. Rev. Lett. **100**, 234505 (2008).
[4] G. Düring, C. Josserand, and S. Rica, Phys. Rev. Lett. **97**, 025503 (2006).
[5] G. Düring, C. Josserand, G. Krstulovic, and S. Rica, Phys. Rev. Fluids **4**, 064804 (2019).
[6] M. Bourgoin, R. Kervil, C. Cottin-Bizonne, F. Raynal, R. Volk, and C. Ybert, Phys. Rev. X **10**, 021065 (2020).
[7] V. Fortov, A. Ivlev, S. Khrapak, A. Khrapak, and G. Morfill, Phys. Rep. **421**, 1 (2005).
[8] A. Piel and A. Melzer, Plasma Phys. Controlled Fusion **44**, R1 (2002).
[9] C. K. Goertz, Rev. Geophys. **27**, 271 (1989).
[10] A. V. Ivlev, A. Burkert, A. Vasyunin, and P. Caselli, Astrophys. J. **861**, 30 (2018).
[11] T. G. Northrop, Phys. Scr. **45**, 475 (1992).
[12] R. L. Merlino, J. Plasma Phys. **80**, 773 (2014).
[13] N. Rao, P. Shukla, and M. Yu, Planet. Space Sci. **38**, 543 (1990).
[14] M. Rosenberg, Planet. Space Sci. **41**, 229 (1993).
[15] R. L. Merlino, A. Barkan, C. Thompson, and N. D'Angelo, Phys. Plasmas **5**, 1607 (1998).
[16] J. Kong, T. W. Hyde, L. Matthews, K. Qiao, Z. Zhang, and A. Douglass, Phys. Rev. E **84**, 016411 (2011).
[17] J. D. Williams, Phys. Rev. E **89**, 023105 (2014).
[18] H.-W. Hu, W. Wang, and L. I, Phys. Rev. Lett. **123**, 065002 (2019).
[19] J. Pramanik, B. Veeresha, G. Prasad, A. Sen, and P. Kaw, Phys. Lett. A **312**, 84 (2003).
[20] E. G. Kostadinova, R. Banka, J. L. Padgett, C. D. Liaw, L. S. Matthews, and T. W. Hyde, Phys. Plasmas **28**, 073705 (2021).
[21] G. Gogia, W. Yu, and J. C. Burton, Phys. Rev. Res. **2**, 023250 (2020).
[22] P.-C. Lin, W.-J. Chen, and L. I, Phys. Plasmas **27**, 010703 (2020).
[23] V. Pandey, P. Perlekar, and D. Mitra, Phys. Rev. E **100**, 013114 (2019).
[24] M. Schwabe, S. Zhdanov, and C. Räth, Phys. Rev. E **95**, 041201(R) (2017).
[25] S. Zhdanov, M. Schwabe, C. Räth, H. M. Thomas, and G. E. Morfill, Europhys. Lett. **110**, 35001 (2015).
[26] S. Zhdanov, C.-R. Du, M. Schwabe, V. Nosenko, H. M. Thomas, and G. E. Morfill, Europhys. Lett. **114**, 55002 (2016).
[27] E. G. Kostadinova, J. L. Padgett, C. Liaw, L. S. Matthews, and T. W. Hyde, in *61st Annual Meeting of the APS Division of Plasma Physics, Fort Lauderdale, Florida* (Bulletin of the American Physical Society, 2016), Vol. 64, abstract no. BAPS.2019.DPP.NO4.10.
[28] J. D. Williams, IEEE Trans. Plasma Sci. **44**, 562 (2016).
[29] P. S. Epstein, Phys. Rev. **23**, 710 (1924).
[30] R. Bedard, S. Lukaschuk, and S. Nazarenko, JETP Lett. **97**, 459 (2013).
[31] G. V. Kolmakov, A. A. Levchenko, M. Y. Brazhnikov, L. P. Mezhov-Deglin, A. N. Silchenko, and P. V. E. McClintock, Phys. Rev. Lett. **93**, 074501 (2004).
[32] L. Deike, M. Berhanu, and E. Falcon, Phys. Rev. E **85**, 066311 (2012).
[33] L. Skrbek, D. Schmoranzer, Š. Midlik, and K. R. Sreenivasan, Proc. Natl. Acad. Sci. U.S.A. **118**, e2018406118 (2021).
[34] J. Jiménez, Phys. Fluids **25**, 101302 (2013).
[35] A. R. Dobrovolskis, J. S. Dacles-Mariani, and J. N. Cuzzi, J. Geophys. Res.: Planets **104**, 30805 (1999).
[36] M. L. Goldstein, R. T. Wicks, S. Perri, and F. Sahraoui, Philos. Trans. R. Soc., A **373**, 20140147 (2015).
[37] R. Kulsrud and W. P. Pearce, Astrophys. J. **156**, 445 (1969).
[38] K. Silsbee, A. V. Ivlev, and M. Gong, Astrophys.J. **922**, 10 (2021).
[39] R. Bintanja, Boundary-Layer Meteorology **95**, 343 (2000).
[40] H. Akbari, J. W. LaBelle, and D. L. Newman, Frontiers in Astronomy and Space Sciences **7**, 617792 (2021).
[41] H. M. Thomas, G. E. Morfill, V. E. Fortov, A. V. Ivlev, V. I. Molotkov, A. M. Lipaev, T. Hagl, H. Rothermel, S. A. Khrapak, R. K. Suetterlin, M. Rubin-Zuzic, O. F. Petrov, V. I. Tokarev, and S. K. Krikalev, New J. Phys. **10**, 033036 (2008).
[42] H. M. Thomas, M. Schwabe, M. Y. Pustylnik, C. A. Knapek, V. I. Molotkov, A. M. Lipaev, O. F. Petrov, V. E. Fortov, and S. A. Khrapak, Plasma Phys. Controlled Fusion **61**, 014004 (2019).
[43] P. Bajaj, S. Khrapak, V. Yaroshenko, and M. Schwabe, Phys. Rev. E **105**, 025202 (2022).
[44] C. R. Du, H. M. Thomas, A. V. Ivlev, U. Konopka, and G. E. Morfill, Phys. Plasmas **17**, 113710 (2010).
[45] L. F. Richardson, Proceedings of the Royal Society of London. Series A, Containing Papers of a Mathematical and Physical Character **110**, 709 (1926).
[46] B. Liu, J. Goree, V. Nosenko, and L. Boufendi, Phys. Plasmas **10**, 9 (2003).
[47] N. Wiener, Acta Mathematica **55**, 117 (1930).
[48] D. C. Champeney, Power spectra and wiener's theorems, in *A Handbook of Fourier Theorems* (Cambridge University Press, Cambridge, UK, 1987), p. 102–117.
[49] A. Khintchine, Math. Ann. **109**, 604 (1934).
[50] A. Einstein, Archives des Sciences **37**, 254 (1914).
[51] D. Allan, T. Caswell, N. Keim, and C. van der Wel, trackpy: Trackpy v0.3.2 (2016), https://doi.org/10.5281/zenodo.60550.
[52] See Supplemental Material at http://link.aps.org/supplemental/10.1103/PhysRevE.107.064603 for the energy spectrum of the other wave phase than shown in Fig. 2 in this paper.
[53] Y. Feng, J. Goree, and B. Liu, Accurate particle position measurement from images. Rev. Sci. Instrum. **78**, 053704 (2007)
[54] D. Mohr, C. Knapek, P. Huber, and E. Zaehringer, J. Imaging. **5**, 30 (2019).